REGULAR PAPER

Improving axial resolution of medical ultrasound images by using noise-robust broadband filter based on singular value decomposition

Japanese Journal of Applied Physics **61**, SG1061 (2022) **REGULAR PAPER**
https://doi.org/**10.35848/1347-4065/ac5a2c**

Improving axial resolution of medical ultrasound images by using noise-robust broadband filter based on singular value decomposition

Kenta Kawamata[1], Shohei Mori[2*], Mototaka Arakawa[1,2], and Hiroshi Kanai[1,2]

[1]*Graduate School of Biomedical Engineering, Tohoku University, Sendai 980-8579, Japan*
[2]*Graduate School of Engineering, Tohoku University, Sendai 980-8579, Japan*

[*]E-mail: shohei.mori.a2@tohoku.ac.jp

Received November 2, 2021; revised February 25, 2022; accepted March 2, 2022; published online May 31, 2022

Improving spatial resolution is a crucial issue in medical ultrasound. One of the improving methods is the post-processing of the received ultrasound RF signal. In the present paper, we proposed a design method for a noise-robust broadband filter based on the singular value decomposition of the received RF signal. To design a noise-robust filter, we proposed a logical method to determine the optimal truncated order of singular values, which was validated by applying the filter to noise-contaminated signals. Furthermore, the proposed filter applied to the wire phantom resulted in a better axial resolution than that obtained without the filter and with our previously designed Wiener filter.

1. Introduction

Ultrasound diagnosis is superior to other diagnostic modalities in terms of real-time use and non-invasiveness, and it is inexpensive. Therefore, it is useful in repeated diagnoses. However, the image resolution of diagnostic ultrasound systems is more degraded than the other modalities; therefore, improving the spatial resolution has been an important issue in the observation of tissue structures in vivo. Recently, ultrasound systems have been applied for the observation of microscopic biological tissues such as the structures of myocardial fiber.[1–4] Improving the spatial resolution in ultrasound imaging will expand the possibilities of ultrasound diagnosis. The determinants of the spatial resolution in ultrasound systems depend on the bandwidth around the center frequency and the aperture size of the transducer. The axial resolution of a general-purpose ultrasound system is mainly determined by the ultrasound wavelength; for example, it is approximately 0.4 mm when four cycles of a 7.5 MHz pulse wave are typically transmitted.

Many methods have been developed to improve spatial resolution. One of these methods is the spatial compounding method.[5–7] This is an image-synthesizing method that uses different images obtained by emitting ultrasound beams with different angles to the same region. Therefore, the method requires the acquisition of multiple images, which deteriorates the temporal resolution.

Many other methods for improving the spatial resolution in signal post-processing have also been proposed. For example, pulse compression,[8,9] frequency-domain processing,[10,11] deconvolution techniques,[12–17] and inversed filtering.[18–25] In our previous study,[26] Kageyama et al. designed a Wiener filter[27] by estimating the signal-to-noise ratio (SNR) from the received RF signals in the frequency domain. As the result, an improvement in the measurement accuracy of the intima-media complex thickness of the posterior wall of the carotid artery has been attained.

In the present study, we propose a method to design a noise-robust broadband filter based on the singular value decomposition (SVD), which is a type of principal component analysis and is often compared with digital Fourier transform (DFT), which is a linear decomposition in the frequency domain. SVD can be used for various purposes because the singular value distribution obtained by SVD represents the features of the received RF signal. SVD has been widely used in medical ultrasound, especially in the field of blood flow imaging.[28–36] When SVD is used to identify artifacts or blood flow components from the acquired signal,[37–39] the spatial information of the signal and the temporal information in the frame direction are separated. In the present study, because the purpose is to improve the axial resolution of medical ultrasound images, only the information of the signal in the beam (depth) direction for a single frame is used for SVD.

When SVD is used for broadband filtering, the singular values must be truncated in an appropriate order to suppress noise components. The truncated singular value decomposition (TSVD) has been widely used in medical ultrasound, for example, to reduce artifacts[37] and to identify blood flow components.[38,39] However, the determination of the truncated order of singular values remains a difficult challenge. Various methods have been proposed to determine the truncated order depending on the purpose of using TSVD; the L-curve method[40,41] and the generalized cross-validation method[42] are commonly known as the properties of Tikhonov's regularized solution and have been widely used not only in the ultrasonic field. The stored energy of singular values[33] and the covariance matrix of singular values[28] are often used to identify blood flow components and reduce artifacts.

We aim to design a broadband filter that is robust to noise. Therefore, we examined a method for logically determining the truncated order of the singular values according to the SNR through simulation experiments in which noise is contaminated on the waveform acquired for the wire.[43] However, in our previous study,[43] the proposed method for the filter design has not been fully validated, that is, the propagation attenuation of ultrasound in each filtering target has not been considered, and the method for evaluating the SNR of the target has not been proposed.

In the present paper, we proposed a design method for a noise-robust filter for high-axial resolution observation using TSVD and proposed a logical method to determine the optimal truncated order of the singular values. The designed filter was applied to the ultrasound received signals from the wire phantom, and the axial resolution due to the filter performance was quantitatively evaluated by the full width at half maximum (FWHM).

2. Principles and filter designing

2.1. Measurement of the transfer function of the ultrasonic transmission/reception system

A block diagram of the ultrasonic transmission/reception system is shown in Fig. 1. When a transfer function $h_d(n)$ is used in the filtering process, a point spread function (PSF) is often defined as the transfer function[18,20] based on the following principle, where n denotes the discrete time. From Fig. 1, the observed received signal $y_d(n)$ from an object at depth d [mm] is expressed as follows:

$$\begin{aligned} y_d(n) &= z_d(n) + e_d(n) \\ &= x_d(n) * h_d(n) * \alpha_d(n) + e_d(n), \end{aligned} \tag{1}$$

where * denotes the convolution operation; $z_d(n)$ is the received signal without contamination owing to the noise component $e_d(n)$; $x_d(n)$ is the true reflectivity, and $\alpha_d(n)$ is the propagation attenuation of ultrasound for the measurement target.

When the target is a wire positioned at a depth d in water, the SNR can be assumed to be sufficiently high. Furthermore, when the diameter of the wire is sufficiently small compared with the wavelength of the transmitted wave, $x_d(n)$ can be assumed to be an impulse $\delta(n)$. That is,

$$e_d(n) \approx 0, \tag{2}$$

$$x_d(n) = \delta(n - d). \tag{3}$$

By substituting Eqs. (2) and (3) into Eq. (1),

$$\begin{aligned} y_{\mathrm{wire},d}(n) &= z_{\mathrm{wire},d}(n) \\ &= \delta(n - d) * h_d(n) * \alpha_d(n) \\ &= h_d(n - d) * \alpha_d(n), \end{aligned} \tag{4}$$

where $y_{\mathrm{wire},d}(n)$ and $z_{\mathrm{wire},d}(n)$ correspond to $y_d(n)$ and $z_d(n)$ of Eq. (1), respectively. The PSF is defined as the transfer function $h_d(n)$ and is obtained from the received signal $y_{\mathrm{wire},d}(n)$ as described below.

2.2. Designing of broadband filter based on SVD

We aim to design a filter so that the filtered signal becomes an impulse. However, this filter amplifies the noise component at the same time. Therefore, we designed a filter to improve the axial resolution while suppressing noise.

First, it is necessary to consider the propagation attenuation $\alpha_d(n)$ for the received signal $y_{\mathrm{wire},d}(n)$ from the wire at a depth d since the received signal $y_d(n)$ is convolved with $\alpha_d(n)$ as shown in Eq. (1). The received signal $y'_{\mathrm{wire},d}(n)$ after compensating for $\alpha_d(n)$ is obtained as follows:

The propagation attenuation $\alpha_d(n)$ is depth-dependent and exhibits a frequency response. The frequency response of the propagation attenuation, $A_d(f)$, is defined by the Fourier transform of $\alpha_d(n)$ as,

$$A_d(f) = \mathrm{DFT}[\alpha_d(n)], \tag{5}$$

where f [MHz] denotes the frequency. The received signal $y_{\mathrm{wire},d}(n)$ from the wire is Fourier transformed, and its frequency spectrum $Y_{wire,d}(f)$ is compensated by $A_d(f)$ in the frequency domain as

$$Y'_{wire,d}(f) = Y_{wire,d}(f) \cdot A_d(f), \tag{6}$$

where $Y'_{wire,d}(f)$ is the corrected frequency characteristics of the RF signal of the wire, and $A_d(f)$ is given by[44]

$$\begin{aligned} A_d(f) &= e^{-8.686 \cdot A \cdot d \cdot f} \\ &= 10^{-A \cdot d \cdot f}, \end{aligned} \tag{7}$$

where $8.686 = 20(\log_{10} e)$, and A [dB/(mm·MHz)] is the attenuation coefficient in the medium along to the pathway to the measurement target. Then, the inverse Fourier transform is applied to obtain the compensated RF signal $y'_{\mathrm{wire},d}(n)$ as

$$y'_{wire,d}(n) = \mathrm{IDFT}[Y'_{wire,d}(f)]. \tag{8}$$

Next, to convolve the filter with $y'_{\mathrm{wire},d}(n)$ in a vector-matrix form, let us define a $(2N + 1) \times (2M + 1)$ matrix $\mathbf{Y}_{\mathrm{wire},d}$, where $y'_{\mathrm{wire},d}(n)$ is converted into an analytic signal by the Hilbert transform in advance and $\{y'_{\mathrm{wire},d}(n)\}$ are arranged by shifting the sample points one by one, as shown in Fig. 2. Thus, the element at the ith row and jth column $(0 \leqslant i \leqslant 2N,\ 0 \leqslant j \leqslant 2M,\ N > M)$ of $\mathbf{Y}_{\mathrm{wire},d}$ is given by

$$\mathbf{Y}_{\mathrm{wire},d}(i, j) = y'_{\mathrm{wire},d}(p - M - N + i + j), \tag{9}$$

where p is the positive peak position of $y'_{\mathrm{wire},d}(n)$. To design the $(2M + 1)$-dimensional filter vector $\mathbf{f}_d$, the height $2N + 1$ of $\mathbf{Y}_{\mathrm{wire},d}$ should be set to a size that allows the filter to be convolved with the entire range of echoes from the wire at a depth d, that is, $M + L_h + 1 < N$, where $2L_h + 1$ is the

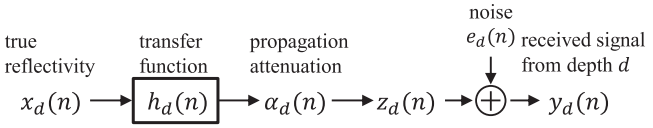

Fig. 1. Block diagram of the ultrasonic transmission/reception system in the time domain.

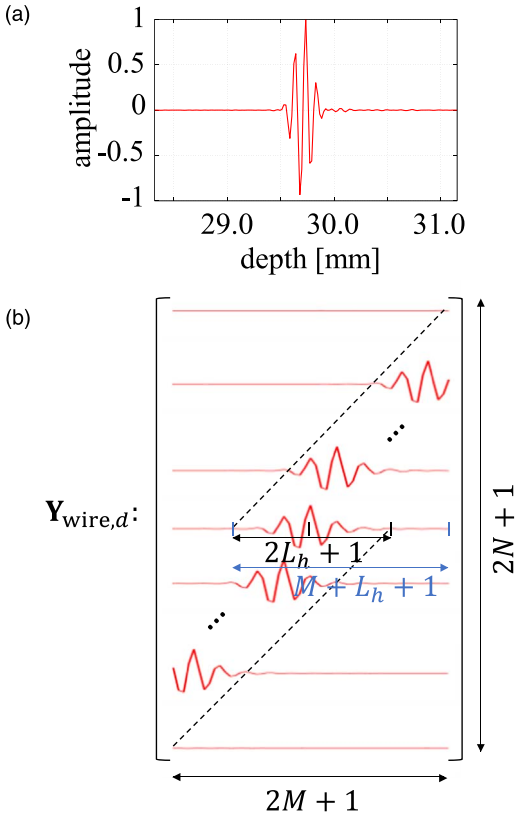

Fig. 2. (Color online) (a) Received RF signal of thin wire and (b) storage method of $\mathbf{Y}_{\mathrm{wire},d}$.

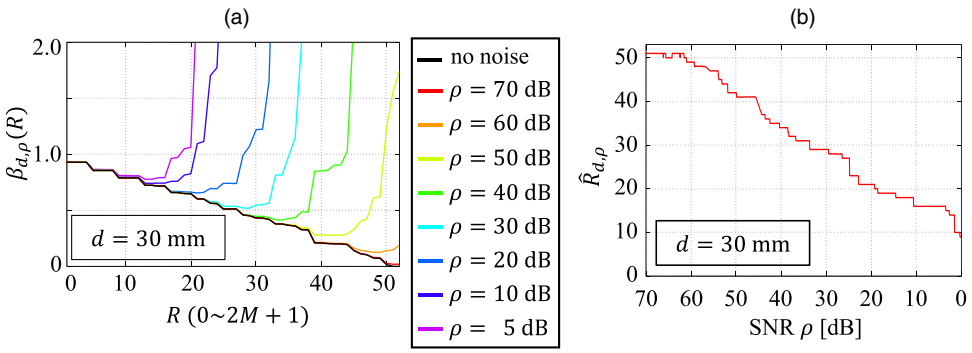

Figure 3. (Color online) (a) Evaluation index $\beta_{d,\rho}(R)$ of the noise robustness of the filter to determine the optimal truncated order and (b) determined optimal truncated order $\hat{R}_{d,\rho}$ of singular values for each SNR ρ at depth d = 30 mm.

effective length of the impulse response $h_d(n)$, as shown in Fig. 2.

As described at the beginning of Sect. 2.2, since we aim for the filtered signal to be impulsive, a $(2N+1)$-dimensional model vector $\mathbf{m}_d$ of an ideal impulse is prepared as an output model. Moreover, since the average power of the signal should not be changed without or with the filter, the amplitude of the output impulse is defined by

$$\mathbf{m}_d(i) = \begin{cases} \dfrac{1}{2M+1}\sqrt{\displaystyle\sum_{n=p-M}^{p+M}[y'_{\mathrm{wire},d}(n)]^2} & (i = N+1) \\ 0 & (i \neq N+1) \end{cases}. \tag{10}$$

That is, the root of the average power of $y'_{\mathrm{wire},d}(n)$ around $n = p$ is set as the amplitude of $\mathbf{m}_d$ at the center position of $i = N+1$ in the row direction.

The filter vector $\mathbf{f}_d$, which is applied at depth d, is designed to minimize the following squared error γ_d between the filtered output waveform $\mathbf{Y}_{\mathrm{wire},d}\mathbf{f}_d$ from the impulse model vector $\mathbf{m}_d$:

$$\gamma_d = |\mathbf{Y}_{\mathrm{wire},d}\mathbf{f}_d - \mathbf{m}_d|^2. \tag{11}$$

Using the least-squares method, the filter $\hat{\mathbf{f}}_d$ that minimizes γ_d is given by

$$\hat{\mathbf{f}}_d = \mathbf{V}\boldsymbol{\Sigma}^{-1}\mathbf{U}^{\mathrm{H}}\mathbf{m}_d, \tag{12}$$

where $\mathbf{U}$ and $\mathbf{V}$ are the $(2N+1)\times(2N+1)$ unitary matrix of the left singular vectors and the $(2M+1)\times(2M+1)$ unitary matrix of right singular vectors, respectively, obtained by SVD of $\mathbf{Y}_{\mathrm{wire},d}$, that is,

$$\mathbf{Y}_{\mathrm{wire},d} = \mathbf{U}\boldsymbol{\Sigma}\mathbf{V}^{\mathrm{H}}, \tag{13}$$

where $\boldsymbol{\Sigma}$ is a $(2N+1)\times(2M+1)$ matrix given by

$$\boldsymbol{\Sigma} = \begin{bmatrix} \boldsymbol{\Delta} \\ \mathbf{O} \end{bmatrix}, \tag{14}$$

$\boldsymbol{\Delta}$ is a $(2M+1)\times(2M+1)$ diagonal matrix with $\sigma_1, \sigma_2, \ldots, \sigma_{2M+1}$ for diagonal elements, and the $[2(N-M)]\times(2M+1)$ matrix $\mathbf{O}$ is a zero matrix. The j th diagonal element σ_j of $\boldsymbol{\Delta}$ is a singular value, and is a positive real number ordered as $\sigma_1 \geqslant \sigma_2 \geqslant \cdots \geqslant \sigma_{2M+1} \geqslant 0$.

When all orders of the singular values are used for the filter design, the resultant filter $\hat{\mathbf{f}}_d$ becomes the filter obtained from the inverse of the PSF and the axial resolution with the filter improves. At the same time, however, a filter with such high truncate order is unstable to noise because the high-order singular values are dominated by noise components. Thus, the singular values should be truncated by an appropriate order considering this trade-off relationship so that the noise components are suppressed and the resultant impulse component becomes a broad frequency range to improve the axial resolution.

Thus, let us introduce a $(2M+1)\times(2N+1)$ matrix $\boldsymbol{\Sigma}_R^{-1}$ where the components higher than the order R are truncated to zero in $\boldsymbol{\Sigma}^{-1}$ as follows:

$$\sum\nolimits_R^{-1}(i,j) = \begin{cases} 1/\sigma_{i,j}\ (1 \leqslant i = j \leqslant R) \\ 0 \qquad (R+1 \leqslant i = j \leqslant 2M+1). \\ 0 \qquad (i \neq j) \end{cases} \tag{15}$$

Substituting $\boldsymbol{\Sigma}_R^{-1}$ into $\boldsymbol{\Sigma}^{-1}$ in Eq. (12), the $(2M+1)$-dimensional filter $\hat{\mathbf{f}}_{d,R}$ is determined such that the singular values of the order higher than R are truncated as

$$\hat{\mathbf{f}}_{d,R} = \mathrm{V}\sum\nolimits_R^{-1}\mathbf{U}^{\mathrm{H}}\mathbf{m}_d, \tag{16}$$

which shows a filter that emphasizes only the components below the truncated order R and suppresses the components above R.

Let us define the $(2N+1)\times(2M+1)$ matrix $\mathbf{Y}_{\mathrm{target},d}$, which stores the received RF signals to be filtered in the same way as $\mathbf{Y}_{\mathrm{wire},d}$ in Eq. (9). By applying the filter $\hat{\mathbf{f}}_{d,R}$ designed around depth d, the $(2N+1)$-dimensional output vector $\boldsymbol{y}'_{\mathrm{out},d}$ is given by

$$\boldsymbol{y}'_{\mathrm{out},d} = \mathbf{Y}_{\mathrm{target},d}\hat{\mathbf{f}}_{d,R}. \tag{17}$$

To compensate for the sound pressure characteristics of the received RF signal owing to the depth, $\boldsymbol{y}'_{\mathrm{out},d}$ is normalized by the spatially averaged power around d of the received RF signal $\boldsymbol{y}_d$ as

$$\boldsymbol{y}_{\mathrm{out},d} = \left(\frac{\mathrm{E}[|\boldsymbol{y}_d|^2]}{\mathrm{E}[|\boldsymbol{y}'_{\mathrm{out},d}|^2]}\right)\boldsymbol{y}'_{\mathrm{out}\prime d}. \tag{18}$$

The $(2N+1)L$-dimensional final output waveform vector $\boldsymbol{y}_{\mathrm{out}}$ along the ultrasonic beam is obtained by arranging $\{\boldsymbol{y}_{\mathrm{out},d}\}$ obtained for L sections along the depth direction as

$$\boldsymbol{y}_{\mathrm{out}} = \begin{bmatrix} \boldsymbol{y}_{\mathrm{out},d_1} \\ \boldsymbol{y}_{\mathrm{out},d_2} \\ \vdots \\ \boldsymbol{y}_{\mathrm{out},d_L} \end{bmatrix}, \tag{19}$$

where L denotes the number of sections.

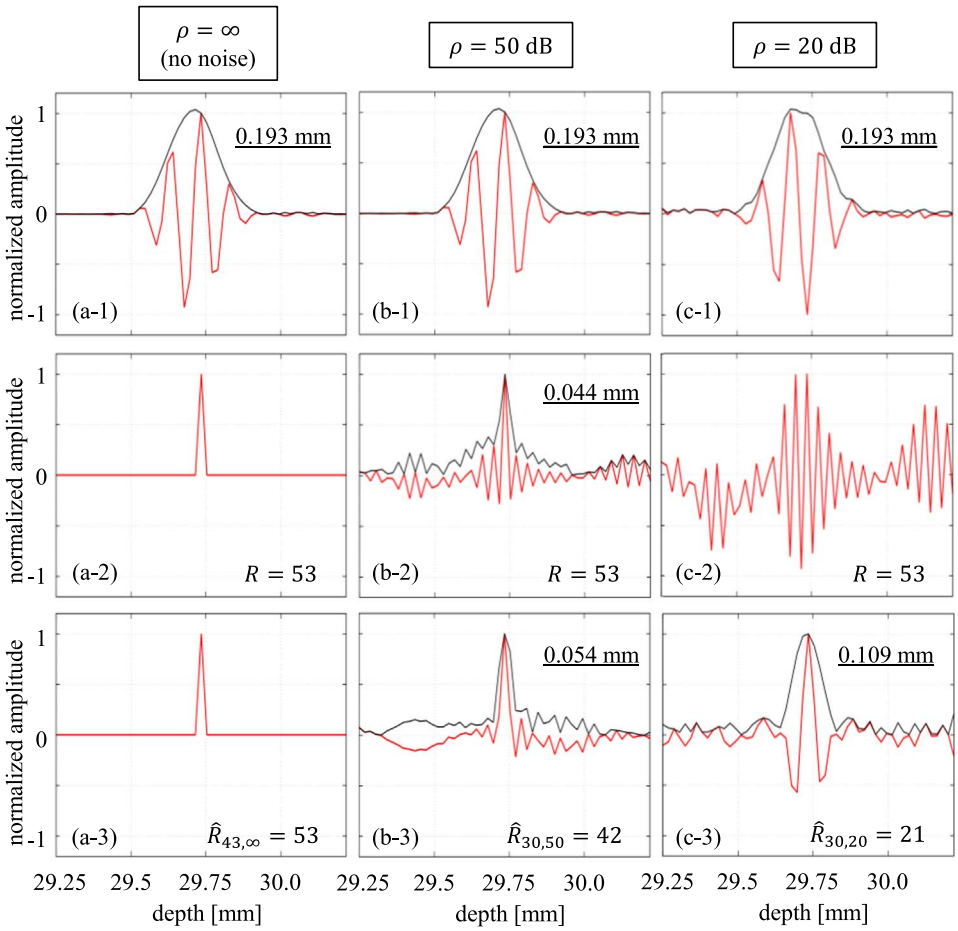

Fig. 4. (Color online) (1) Waveforms without the filter, (2) output waveforms when the singular value was used with the full rank, and (3) output waveforms when the singular value was truncated at the optimal order by the proposed method, where (a) noise was not contaminated, (b) $\rho = 50$ dB, and (c) $\rho = 20$ dB at depth $d = 30$ mm. (The underlined numbers in the figure indicate the FWHM.)

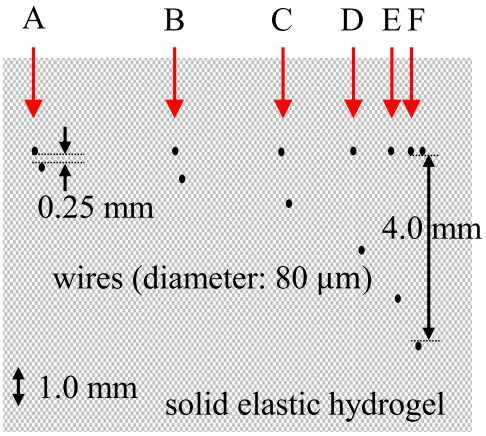

Fig. 5. (Color online) Structure of the wire phantom.

2.3. Logical method for determining the truncated order of singular values

As described in Sect. 2.2, the high-order singular values of $\mathbf{Y}_{\text{wire},d}$ are dominated by noise components. Thus, we propose a logical method to determine the optimal truncated order $\hat{R}_{d,\rho}$ of the singular values considering the SNR ρ_{target} of the measurement target at a depth d as follows:

To consider the SNR ρ, the noise-contaminated signal $y_{\text{noisy},d,\rho,q}(n)$ is generated by adding the Gaussian white noise $e_{\rho,q}(n)$ on $y'_{\text{wire},d}(n)$:

$$y_{\text{noisy},d,\rho,q}(n) = y'_{\text{wire},d}(n) + e_{\rho,q}(n), \tag{20}$$

where Q sets of the white noises $\{e_{\rho,q}(n)\}$ were independently generated on the computer for each SNR ρ, and q ($q = 1 \sim Q$) shows the set number of the generated white noises. Let us prepare a $(2N+1) \times (2M+1)$ matrix $\mathbf{Y}_{\text{noisy},d,\rho,q}$ which stores the noise-contaminated signal $y_{\text{noisy},d,\rho,q}(n)$ in the same way as the matrix $\mathbf{Y}_{\text{wire},d}$ of Fig. 2(b) as

$$\mathbf{Y}_{\text{noisy},d,\rho,q}(i,j) = y_{\text{noisy},d,\rho,q}(p - M - N + i + j). \tag{21}$$

Then, we define the set of the following index $\beta_{d,\rho}(R)$ for each depth d and each SNR ρ to evaluate the noise robustness of the designed filter:

$$\beta_{d,\rho}(R) = \mathrm{E}_q[|\mathbf{Y}_{\text{noisy},d,\rho,q}\,\hat{\mathbf{f}}_{d,R} - \mathbf{m}_d|^2], \tag{22}$$

where $\mathrm{E}_q[\cdot]$ shows the average operation on q, and $\beta_{d,\rho}(R)$ evaluates the mean squared difference of the result of applying the filter $\hat{\mathbf{f}}_{d,R}$ to $\mathbf{Y}_{\text{noisy},d,\rho,q}$ from the ideal impulse model $\mathbf{m}_d$. The designed filter $\hat{\mathbf{f}}_{d,R}$ is robust to noise if $\beta_{d,\rho}(R)$ is small. Thus, the optimal truncated order $\hat{R}_{d,\rho}$ is determined

to minimize $\beta_{d,\rho}(R)$ as follows:

$$\hat{R}_{d,\rho} = \underset{R}{\operatorname{argmin}}\, \beta_{d,\rho}(R). \tag{23}$$

In this procedure, $\hat{R}_{d,\rho}$ is independently determined for each depth d and each SNR ρ.

Gaussian white noise was generated on the computer using the Box–Muller method,[45] and the number Q of trials to generate white noise was set to 200. The power of the generated white noise $e_{\rho,q}(n)$ in Eq. (20) was set such that the SNR ρ ranged from 0 to 70 dB with 0.05 dB interval and $\hat{R}_{d,\rho}$ was determined for each ρ.

Figure 3(a) shows the evaluation index $\beta_{d,\rho}(R)$ of the noise robustness of the filter calculated for wires at depth $d = 30$ mm. As shown in Fig. 3(a), $\beta_{d,\rho}(R)$ rapidly increased for R beyond $\hat{R}_{d,\rho}$. This confirms that the filtered result was sensitive to noise and it was important to determine the optimal truncated order $\hat{R}_{d,\rho}$ in the filter design.

Figure 3(b) shows the optimal truncated order $\hat{R}_{d,\rho}$ for various SNR ρ at depth $d = 30$ mm. As shown in Fig. 3(b), $\hat{R}_{d,\rho}$ approximately linearly shifted to lower orders as the SNR ρ logarithmically decreased. Thus, it is important to truncate the singular values at different orders $\hat{R}_{d,\rho}$ according to the SNR ρ.

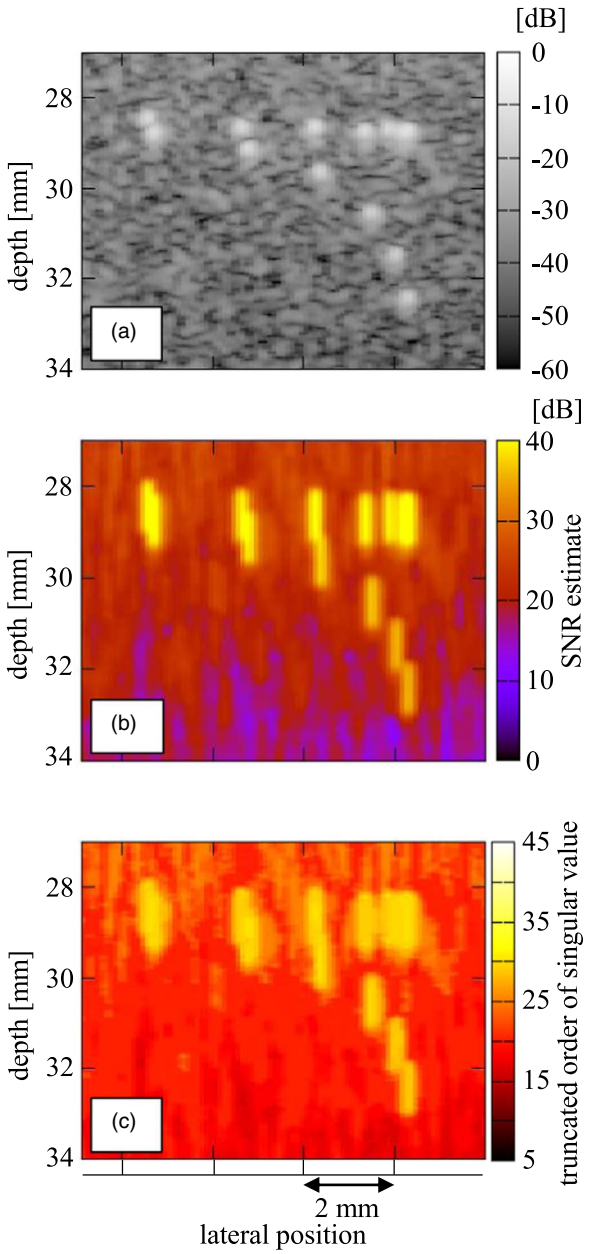

Fig. 6. (Color online) (a) B-mode image of the wire phantom, (b) evaluated result of SNR ρ_{target}, and (c) optimal truncated order $\hat{R}_{d,\rho_{\text{target}}}$ estimated based on the SNR ρ.

2.4. Method for evaluating SNR in actual case

In the proposed method, the truncated order $\hat{R}_{d,\rho_{\text{target}}}$ is determined locally and adaptively according to the SNR ρ_{target} of the filtering target. In this section, we describe a method for the evaluation of the SNR. In the present paper, by assuming that the filtering target is motionless between frames, we evaluate the SNR $\rho(n, k)$ for the received RF signal $y_{j,k}(n)$ of the jth frame along the kth beam to be filtered as follows:

$$\rho(n, k) = 10\log_{10}\frac{P_{\text{S}}(n, k)}{P_{\text{N}}(n, k)}\ [\text{dB}], \tag{24}$$

where

$$P_{\text{S}}(n, k) = \frac{1}{2M+1}\sum_{n'=n-M}^{n+M}(\text{E}_j[y_{j,k}(n')])^2, \tag{25}$$

$$P_{\text{N}}(n, k) = \frac{1}{2M+1}\sum_{\text{n}'=\text{n}-\text{M}}^{\text{n}+\text{M}}\text{E}_j[(y_{j,k}(n') - \text{E}_j[y_{j,k}(n')])^2]. \tag{26}$$

This SNR evaluation is also used for the preliminary determination of the optimal truncated order $\hat{R}_{d,\rho}$ of Eq. (23) for each depth d and SNR ρ. In the filtering procedure, $\rho_{\text{target}}(n, k)$ is estimated by Eq. (24), and then $\hat{R}_{d,\rho_{\text{target}}}$ is determined from Eq. (23) as the optimal truncated order for filtering. When the filter is applied to an object that moves between frames, the SNR evaluation of Eq. (24) should be replaced, which is our future work.

3. Experiments and results

3.1. Filtering for received signal from wire in water

To evaluate the robustness of the designed filter, the designed filter $\hat{\mathbf{f}}_{d,R}$ of Eq. (16) was applied to the received signal $\mathbf{Y}_{\text{wire},d}$ from the wire in the water. A linear probe connected to ultrasound diagnostic equipment (SSD-6500; ALOKA, Japan) was used. The center frequency of the transmitted wave was 7.5 MHz, and the sampling frequency was 40 MHz. The focus was set to a depth of 20 mm. The matrix size of $\mathbf{Y}_{\text{wire},d}$ in the filter design was set to $2N + 1 = 101$ (1.9 mm) and $2M + 1 = 53$ (1.0 mm), that is, the filter length was 53 (1.0 mm). The attenuation in water can be assumed to be zero in the frequency range and depth of the ultrasound used in this experiment.[46]

Figure 4(1) shows the received RF signal $y_{\text{wire},d}(n)$ from a wire and the noise-contaminated signals $y_{\text{noisy},d,50,1}(n)$ and $y_{\text{noisy},d,20,1}(n)$ with SNRs of 50 and 20 dB at depth $d = 30$ mm, respectively. Figure 4(2) shows the waveforms with the filter $\hat{\mathbf{f}}_{d,R}$ obtained with full rank ($R = 53$) of singular values. Figure 4(3) shows the waveform with filter $\hat{\mathbf{f}}_{d,\hat{R}}$ designed by truncating the singular values at the optimal truncated order $\hat{R}_{d,\rho}$. Each envelope is plotted as a black line, and the FWHM is shown in the figure.

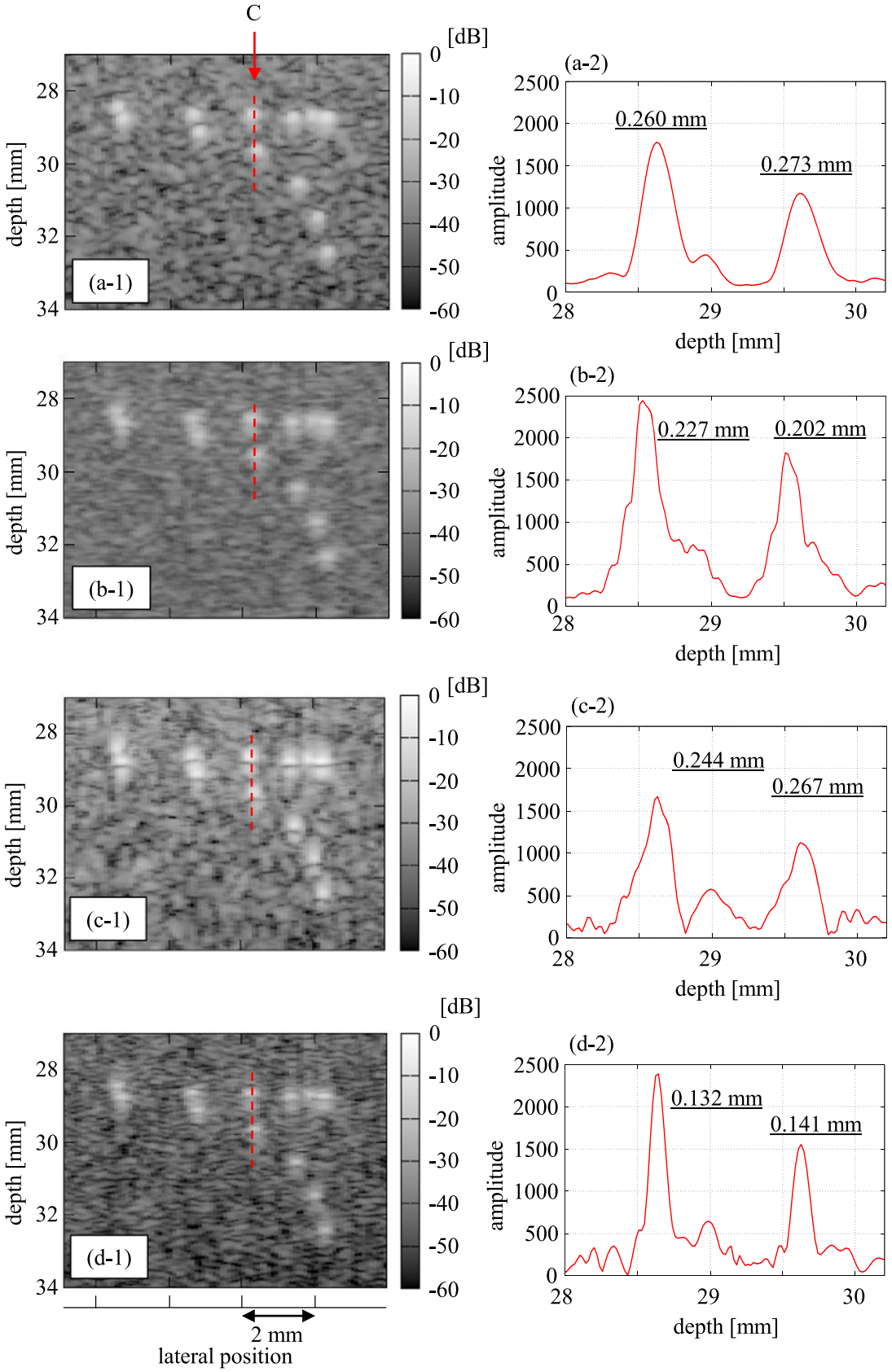

Fig. 7. (Color online) (1) B-mode images and (2) the envelopes of the red dashed line (a) without the filter, (b) with the Wiener filter, (c) with the proposed filter without considering attenuation, and (d) with the proposed filter considering attenuation. (The underlined numbers in the figure indicate the FWHM).

When the noise was not contaminated [Fig. 4(a)], the signal from the wire became an ideal impulse by using the full rank of the singular values [Fig. 4(a-2)]. When the noise was contaminated with $\rho = 20$ dB [Fig. 4(b)], the wire could not be observed at all when the full rank of the singular values was used [Fig. 4(c-2)]. For $\rho = 50$ dB and using the full rank of singular values [Fig. 4(b-2)], the wire could be observed; however, a large noise component appeared in the

Table I. FWHM of the enveloped signals without and with the filter in Fig. 7, and the improvement rate of FWHM compared to the original for the beam C.

	FWHM [mm]	
	Shallower wire (d = 28.6 mm)	Deeper wire (d = 29.6 mm)
(a) Original	0.260 (–)	0.273 (–)
(b) By Wiener filter	0.227 (13%)	0.202 (27%)
(c) By proposed filter without considering attenuation	0.244 (7%)	0.267 (3%)
(d) By proposed filter $\hat{\mathbf{f}}_{30,\hat{R}}$ with considering attenuation	0.132 (49%)	0.141 (49%)

Table II. FWHM of the enveloped signals without and with the proposed filter in Fig. 7, and the improvement rate of FWHM compared to the original for the beams A–F.

		FWHM [mm]	
Beam No.		(a) Original	(b) Proposed filter $\hat{\mathbf{f}}_{30,\hat{R}}$
A	Shallower	0.256 (–)	0.116 (55%)
	Deeper	0.270 (–)	0.134 (51%)
B	Shallower	0.267 (–)	0.134 (50%)
	Deeper	0.250 (–)	0.123 (51%)
C	Shallower	0.260 (–)	0.132 (49%)
	Deeper	0.273 (–)	0.141 (49%)
D	Shallower	0.268 (–)	0.156 (42%)
	Deeper	0.277 (–)	0.165 (41%)
E	Shallower	0.348 (–)	0.144 (59%)
	Deeper	0.279 (–)	0.154 (45%)
F	Shallower	0.270 (–)	0.128 (53%)
	Deeper	0.277 (–)	0.161 (42%)

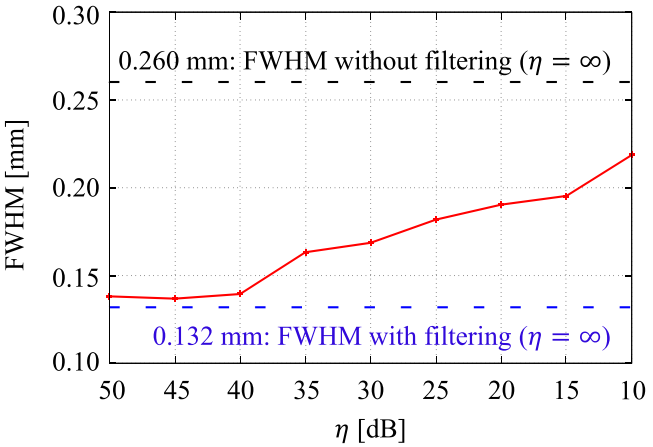

Fig. 9. (Color online) The FWHM of the enveloped signals obtained by the proposed filtering for each SNR η.

surrounding area. On the other hand, even when the noise was contaminated, by truncating the singular values with the optimal truncated order $\hat{R}_{d,\rho}$, the signal from the wire could be observed [Figs. 4(b-3) and 4(c-3)].

By comparing the axial resolution based on the FWHM, it was confirmed that the axial resolution was improved for all SNRs by filtering with the optimal truncated order $\hat{R}_{d,\rho}$ [Fig. 4(3)] compared to that with no filtering [Fig. 4(1)]. As the SNR ρ became low, the singular values must be truncated at a lower order. Therefore, when comparing the axial resolution of Figs. 4(b-3) and 4(c-3), the FWHM of Fig. 4(c-3) was 0.109 mm, which was broader than the FWHM of Fig. 4(b-3) of 0.054 mm. However, even in Fig. 4(c-3), the wire position could be confirmed, and the

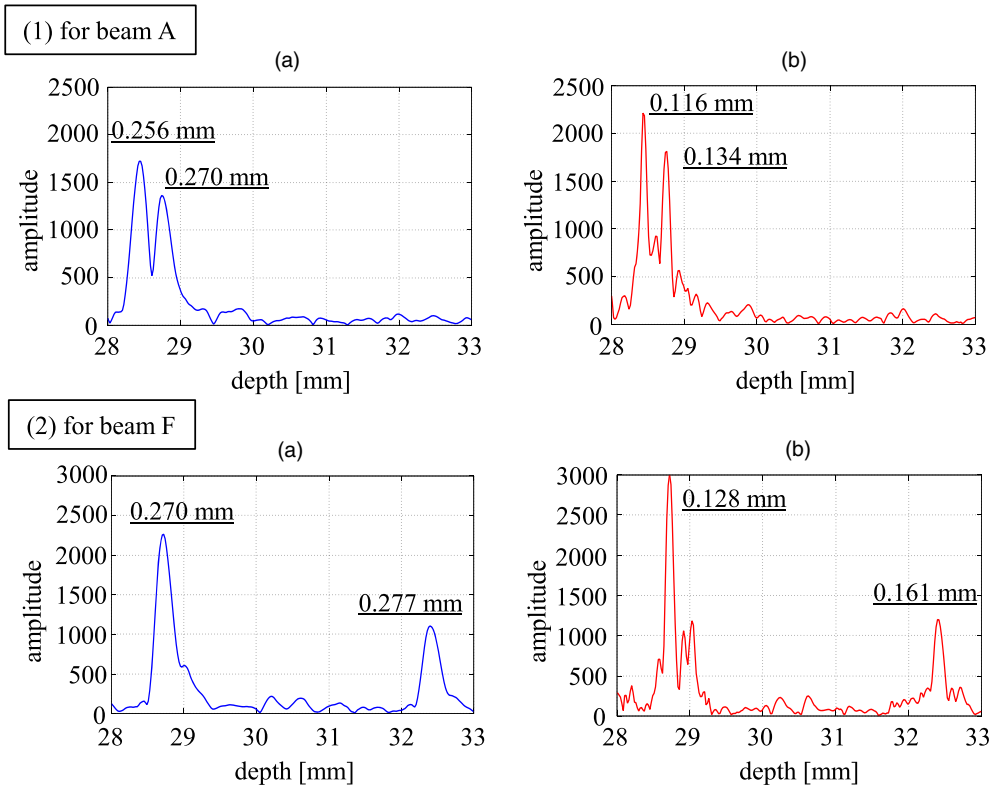

Fig. 8. (Color online) The envelopes (a) without filtering and (b) with the proposed filtering for the beams (1) A and (2) F in Fig. 5.

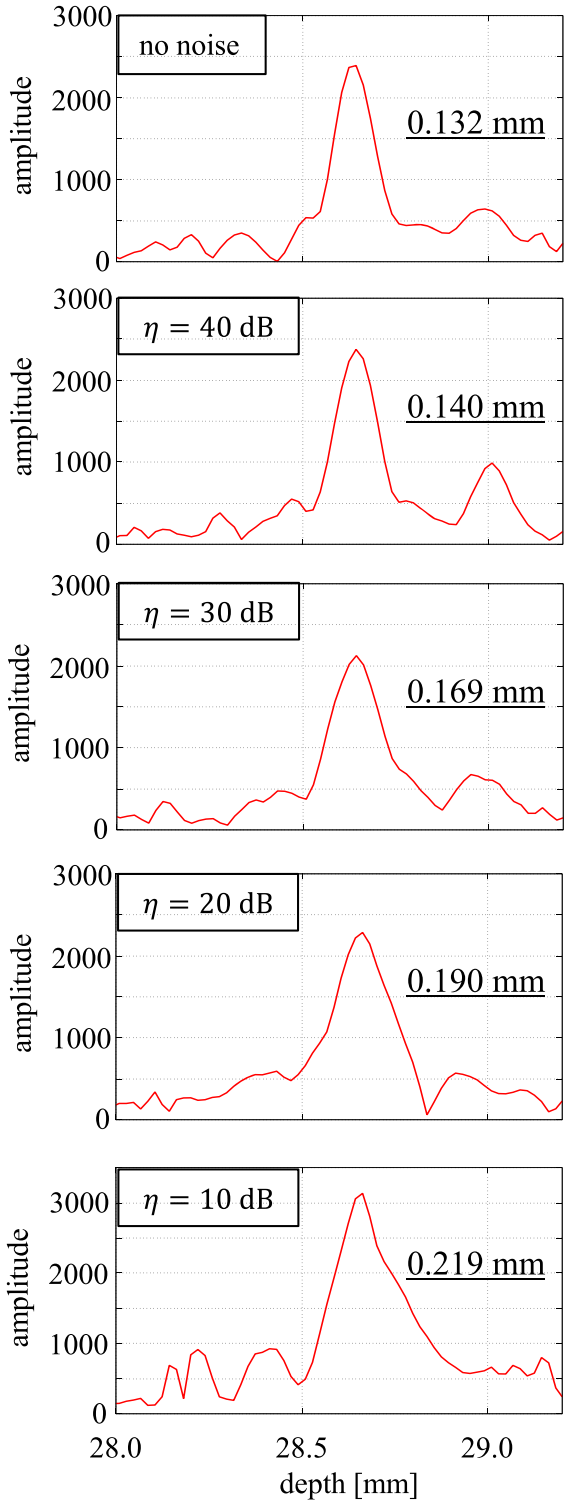

Fig. 10. (Color online) The envelope of the wire echo obtained by the proposed filtering for each of $\eta = \infty$, 40, 30, 20, and 10 dB.

axial resolution was improved compared with Fig. 4(c-1) [the FWHM of Fig. 4(c-1) was 0.193 mm]. Thus, the filter designed by the method in Sects. 2.2 and 2.3 is robust to noise and improves the axial resolution.

3.2. Filtering for received signal from phantom

To evaluate the usefulness of the designed filter $\hat{\mathbf{f}}_{d,\hat{R}}$, the filter was applied to a general purpose ultrasound phantom [Model 054GS by CIRS (USA)]. As shown in Figs. 5, 13 wires were lined up inside the phantom, and the beams A–F shown by the red arrows in Fig. 5 were used for evaluation. The two wires were 0.25 mm apart for beam A and 4.0 mm apart for beam F, respectively. The wire material was nylon with a diameter of 80 μm. The attenuation coefficient A of the phantom was 0.07 dB/(mm·MHz).

When applying the filter, we first evaluated the SNR ρ_{target} of the target, and then we determined the truncated order $\hat{R}_{d,\rho_{\text{target}}}$ by referring to the optimal truncated order $\hat{R}_{d,\rho}$ predetermined for each depth d and SNR ρ as described in Sect. 2.3. The filter $\hat{\mathbf{f}}_{d,\hat{R}}$ designed at a depth of $d = 30$ mm was applied to the phantom data.

Figure 6 shows (a) the B-mode image of the wire phantom, (b) the evaluated SNR ρ_{target} for each depth along each beam, and (c) the determined optimal truncated order $\hat{R}_{d,\rho_{\text{target}}}$ for each depth and beam, respectively. In Fig. 6(b), the SNR was high at the position where the wires existed because the signal intensities from wires were strong. As the depth became deeper, the SNR decreased due to the attenuation of ultrasonic waves. Thus, the SNR was confirmed to be reasonably evaluated using Eq. (24).

In Fig. 6(c), the optimal truncated orders $\hat{R}_{d,\rho_{\text{target}}}$ of the singular values were large at the positions where the SNR was high. This means that the filter was designed using a large number of singular values for regions with a high SNR. Therefore, by determining $\hat{R}_{d,\rho_{\text{target}}}$ for each depth d and each SNR ρ_{target} using our proposed method, the filter was designed by considering the trade-off relationship between the axial resolution improvement and noise suppression.

Figure 7 shows (1) the B-mode images and (2) the envelopes on the red dashed line in the B-mode images (a) without the filter, (b) with the Wiener filter, (c) with the proposed filter without considering attenuation [$\alpha_d(n) = \delta(n)$], and (d) with the proposed filter $\hat{\mathbf{f}}_{30,\hat{R}}$ by considering attenuation, respectively. In the B-mode images, the axial resolutions with the filters (b) and (d) were improved compared to those without the filter. The FWHM of the envelope of the wire echo in Fig. 7(2) is shown in Table I. The axial resolution of the shallower wire at a depth of 28.6 mm was improved by 13% (from 0.260 to 0.227 mm) with the Wiener filter, while it was improved by 49% (from 0.260 to 0.132 mm) with the proposed filter by considering attenuation. For the deeper wire at a depth of 29.6 mm, the Wiener filter improved the axial resolution by 27% (from 0.273 to 0.202 mm), while considering attenuation in the proposed filter improved it by 49% (from 0.273 to 0.141 mm). Thus, it was confirmed that the proposed filter with considering attenuation improved the axial resolution. In the proposed filter without considering attenuation [Fig. 7(c)], the axial resolution of both wires was slightly improved (7% and 3%), which shows that the correction of the high-frequency components is essential to widen the frequency characteristics in the filter design. As shown in Figs. 7(c-2) and 7(d-2), with filtering, some peaks other than those at the wire positions were observed such as at a depth of 29 mm. However, they were already observed without filtering, as shown in Fig. 7(a-2). The cause of this observation will be investigated in more detail in the future.

To observe the improvement of the axial resolution by the proposed filter $\hat{\mathbf{f}}_{30,\hat{R}}$ in more detail, the FWHM and its improvement rate are shown in Table II. The envelopes

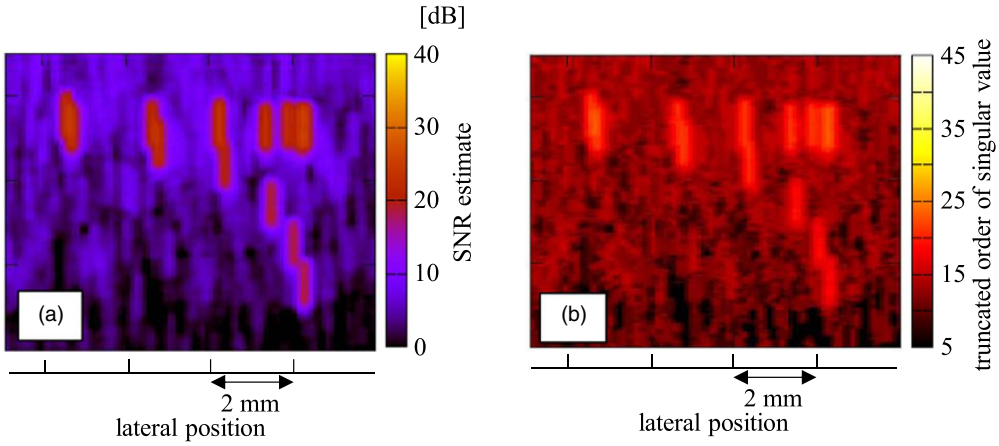

Fig. 11. (Color online) (a) Results of the SNR evaluation and (b) the determined optimal truncated order at $\eta = 30$ dB.

without and with filtering for the beams A and F are shown in Fig. 8. As shown in Table II, the improvement in axial resolution was nearly 50% for all beams, and the discrimination capability of wires was improved as shown in Figs. 8(1-b) and 8(2-b).

3.3. Evaluation of the noise robustness of filter

To confirm the noise robustness of the proposed filter, the RF signals received from the phantom in Sect. 3.2 were contaminated with white noise generated on the computer. The power of the noise was set such that the ratio η of the squared average brightness of the shallower wire echoes along the red dashed line in Fig. 7(a-1) to the power of the noise was from 10 to 50 dB (intervals: 5 dB).

Figure 9 shows the FWHM of the wire echo for all η, and Fig. 10 shows the envelope of the wire echo for $\eta = \infty$, 40, 30, 20, and 10 dB. As in the underwater wire experiment in Sect. 3.1, the FWHM decreased as the noise superposition level increased, but for SNRs, the axial resolution was improved compared to that without the filter.

Figures 11(a) and 11(b) show the results of the SNR evaluation and the determined optimal truncated order, respectively, for $\eta = 30$ dB. By comparing Figs. 11(a) and 11(b) for $\eta = 30$ dB to Figs. 6(b) and 6(c) for $\eta = \infty$, the estimated SNR of Eq. (24) decreased as the power of the noise increased, and the optimal truncated orders $\hat{R}_{d,\rho}$ decreased.

Figure 12 shows the B-mode images (a) without the filter, (b) with the Wiener filter, and (c) with the proposed filter for $\eta = 30$ dB, respectively. The FWHM of the envelope of the wire, shown by the red arrow on each B-mode image, is summarized in Table III, where the values in parentheses show the improvement in the axial resolution from that without filtering. In the evaluation of the B-mode images and quantitative evaluation by FWHM, it was confirmed that the proposed filter increased the axial resolution.

As shown in Table III, the improvement rates of the axial resolution for the proposed filter decreased owing to the lowering of the truncated order, which was associated with a lower SNR; however, the improvement in axial resolution was maintained at nearly 40%. However, when the Wiener filter was applied, the improvement rates of the axial resolution significantly decreased with a lower SNR, and the rate was only 3% for $\eta = 30$ dB.

In this study, the optimal truncated order $\hat{R}_{d,\rho}$ was determined for each SNR ρ, and the proposed filter was optimized for each SNR ρ_{target} of the measurement target. Therefore, this filter design can be applied to the low SNR cases. On the other hand, although we designed the Wiener filter considering the SNR of the target, the weighting control parameter, which determined how much the SNR was reflected in the filter design, was fixed to a constant value because a method to determine the parameter had not yet been established.

3.4. Discussion about depth dependence of the proposed filter

Figure 13 shows the superimposition of the received RF signals $\{y_{\text{wire},d}(n)\}$ acquired by placing a tungsten wire with a diameter of 10 μm at a depth d in water and moving the wire in the range from $d = 5$ to 55 mm at an interval of 1 mm. The focus was set to a depth of 20 mm. The amplitudes of the received signals $\{y_{\text{wire},d}(n)\}$ used in the filter design changed in the depth direction due to the sound pressure characteristics.

In the present paper, the filter was designed only for a depth of $d = 30$ mm to focus on the evaluation of the noise robustness of the proposed filter. Although the transfer function of the ultrasonic transmission/reception system is depth-dependent as shown in Fig. 13, the principle of the proposed filter design can be extended and applied at different depths.

4. Conclusions

In the present paper, we proposed a broadband filter based on TSVD to improve the axial resolution of medical ultrasound images. We proposed a logical method to determine the truncated order of the singular values based on the SNR to design a noise-robust filter. Basic experiments targeting wires in water confirmed that the proposed method could be used to design a noise-robust filter. Then, the usefulness of the proposed filter was confirmed through an experiment using a wire phantom as the measurement target. The axial resolution of the proposed filter was improved by 36% on average of the FWHM of the wires in the phantom compared with our previously designed Wiener filter under high SNR conditions. Furthermore, phantom evaluations under lower SNR conditions demonstrated the robustness of the proposed filter.

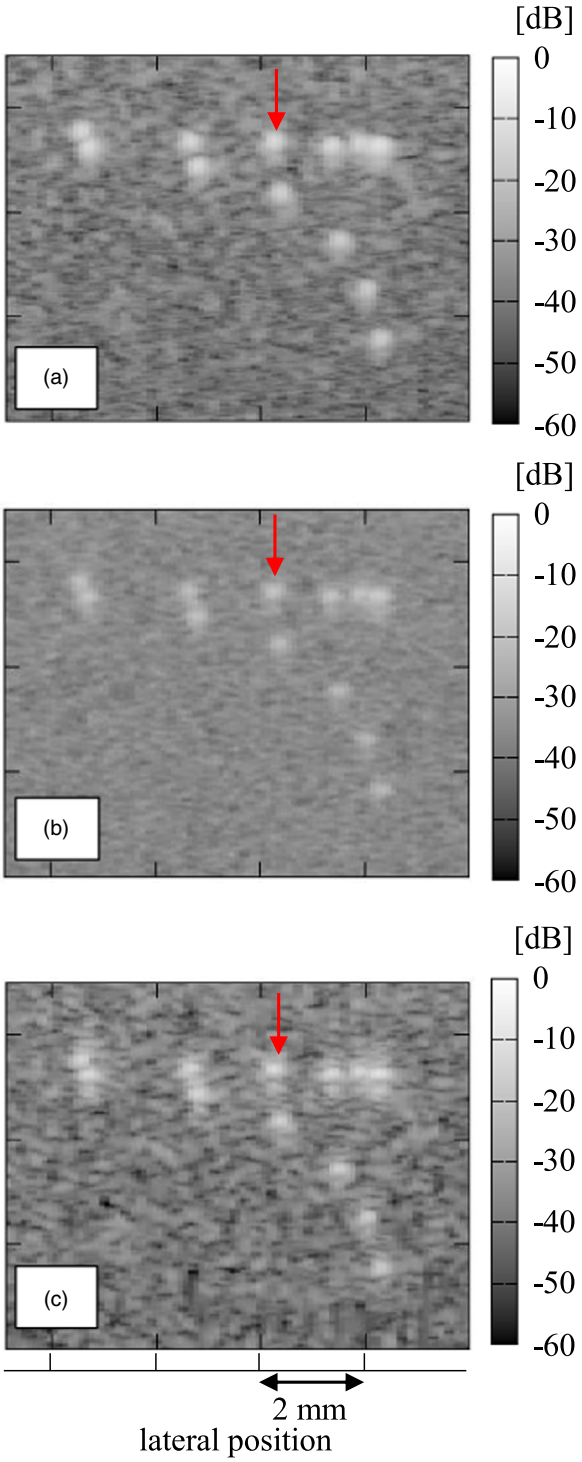

Fig. 12. (Color online) B-mode images (a) without the filter, (b) with the Wiener filter, and (c) with the proposed filter at $\eta = 30$ dB.

Table III. FWHM of the enveloped signals without and with the filter in Fig. 12, and the improvement rate of FWHM compared to the original.

	FWHM [mm]	
	$\eta = \infty$ (no noise)	$\eta = 30$ dB
(a) Original	0.260 (–)	0.266 (–)
(b) By Wiener filter	0.227 (13%)	0.259 (3%)
(c) By proposed filter $\hat{\mathbf{f}}_{30,\hat{R}}$	0.132 (49%)	0.168 (37%)

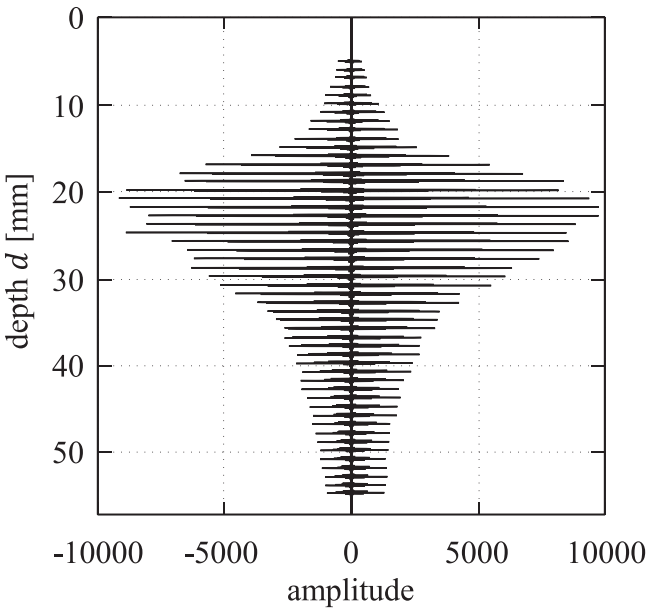

Fig. 13. Received RF signals $\{y_{\text{wire},d}(n)\}$ from the wire in the water.

Acknowledgments

This work was supported in part by JSPS KAKENHI 19KK0100.

ORCID iDs

Shohei Mori https://orcid.org/0000-0002-5494-1055
Mototaka Arakawa https://orcid.org/0000-0001-9386-645X
Hiroshi Kanai https://orcid.org/0000-0002-6567-1687

1) W.-N. Lee, M. Pernot, M. Couade, E. Messas, P. Bruneval, A. Bel, A. A. Hagège, M. Fink, and M. Tanter, IEEE Trans. Med. Imaging **31**, 554 (2012).
2) C. Papadacci, V. Finel, J. Provost, O. Villemain, P. Bruneval, J.-L. Gennisson, M. Tanter, M. Fink, and M. Pernot, Sci. Rep. **7**, 1 (2017).
3) M. L. Milne, B. M. Schick, T. Alkhazal, and C. S. Chung, Ultrason. Med. Biol. **45**, 2075 (2019).
4) M. L. Milne, G. K. Singh, J. Miller, and M. R. Holland, Ultrason. Imaging **34**, 129 (2012).
5) S. Huber, M. Wagner, M. Medl, and H. Czembirek, Ultrasound Med. Biol. **28**, 155 (2002).
6) M. Pernot, M. Tanter, J. Bercoff, K. R. Waters, and M. Fink, IEEE Trans. Ultrason. Ferroelectr. Freq. Control **51**, 606 (2004).
7) J. R. Sanchez and M. L. Oelze, IEEE Trans. Ultrason. Ferroelectr. Freq. Control **56**, 1327 (2009).
8) M. L. Oelze, IEEE Trans. Ultrason. Ferroelectr. Freq. Control **54**, 768 (2007).
9) T. Misaridis and J. A. Jensen, IEEE Trans. Ultrason. Ferroelectr. Freq. Control **52**, 177 (2005).
10) H. Taki, K. Taki, M. Yamakawa, T. Shiina, M. Kudo, and T. Sato, Jpn. J. Appl. Phys. **54**, 07HF05 (2015).
11) H. Taki, T. Sakamoto, M. Yamakawa, T. Shiina, and T. Sato, IEEJ Trans. Electron. Inf. Syst. **132**, 1552 (2012).
12) M. Fatemi and A. C. Kak, Ultrason. Imaging **2**, 1 (1980).
13) G. Demoment, R. Reynaud, and A. Herment, Ultrason. Imaging **6**, 435 (1984).
14) A. Herment, J. P. Guglielmi, P. Dumee, P. Peronneau, and P. Delouche, Ultrasonics **25**, 267 (1987).
15) J. A. Jensen, Ultrason. Imaging **14**, 1 (1992).
16) T. Taxt, IEEE Trans. Ultrason. Ferroelectr. Freq. Control **42**, 543 (1995).
17) J. Chen, E. Wu, H. Wu, H. Zhou, and K. Yang, Ultrasonics **96**, 175 (2019).

18) D. Iracà, L. Landini, and L. Verrazzani, IEEE Trans. Ultrason. Ferroelectr. Freq. Control **36**, 216 (1989).
19) S.-K. Sin and C.-H. Chen, IEEE Trans. Image Process. **1**, 3 (1992).
20) W.-S. Yeoh and C. Zhang, IEEE Trans. Biomed. Eng. **53**, 2001 (2006).
21) C. Dalitz, R. P.- Fröhlich, and T. Michalk, IEEE Trans. Ultrason. Ferroelectr. Freq. Control **62**, 531 (2015).
22) H. Hasegawa, Jpn. J. Appl. Phys. **56**, 07JF02 (2017).
23) M. Mozumi, R. Nagaoka, and H. Hasegawa, Jpn. J. Appl. Phys. **57**, 07LF23 (2018).
24) H. Hasegawa, M. Mozumi, M. Omura, and R. Nagaoka, Jpn. J. Appl. Phys. **60**, SDDE16 (2021).
25) H.-W. Xie, H. Guo, G.-Q. Zhou, N. Q. Nguyen, and R. W. Prager, Ultrasonics **119**, 106594 (2022).
26) S. Kageyama, H. Hasegawa, and H. Kanai, Jpn. J. Appl. Phys. **52**, 07HF04 (2013).
27) N. Wiener, *Extrapolation, Interpolation, and Smoothing of Stationary Time Series* (MIT Press, Cambridge, MA, 1949) 2.
28) H. Ikeda, S. Yoshizawa, M. Maeda, S. Umemura, and Y. Saijo, Jpn. J. Appl. Phys. **58**, SGGE15 (2019).
29) C. Huang, P. Song, P. Gong, J. D. Trzasko, A. Manduca, and S. Chen, IEEE Trans. Ultrason. Ferroelectr. Freq. Control **66**, 1281 (2019).
30) R. R. Wildeboer et al., IEEE Trans. Ultrason. Ferroelectr. Freq. Control **67**, 1497 (2020).
31) W. Guo, Y. Wang, and J. Yu, Appl. Sci. **6**, 359 (2016).
32) S. Feng, Y. Wang, C. Zheng, Z. Han, and H. Peng, Appl. Sci. **10**, 5595 (2020).
33) H. Hasegawa and R. Nagaoka, Jpn. J. Appl. Phys. **58**, SGGE06 (2019).
34) H. Hasegawa, R. Nagaoka, M. Omura, M. Mozumi, and K. Saito, J. Med. Ultrason. **48**, 13 (2021).
35) B. P. Epps and E. M. Krivitzky, Exp. Fluids **60**, 126 (2019).
36) J. Shen and E. S. Ebbini, IEEE Trans. Ultrason. Ferroelectr. Freq. Control **43**, 141 (1996).
37) F. W. Mauldin Jr, D. Lin, and J. A. Hossack, IEEE Trans. Med. Imaging **30**, 1951 (2011).
38) G. C. Collins, B. Jing, and B. D. Lindsey, Ultrasonics **108**, 106200 (2020).
39) C. Demené et al., IEEE Trans. Med. Imaging **34**, 2271 (2015).
40) P. C. Hansen and D. P. O'Leary, SIAM J. Sci. Comput. **14**, 1487 (1993).
41) L. Reichel and H. Sadok, J. Comput. Appl. Math. **219**, 493 (2008).
42) G. H. Golub, M. Heath, and G. Wahba, Technometrics **21**, 215 (1979).
43) K. Kawamata, S. Mori, M. Arakawa, and H. Kanai, Proc. 42nd Symp. on Ultrasonic Electronics, 3Pa5-3, 2021.
44) B. A. Auld, *Acoustic Fields and WAVES in Solids* (Wiley, New York, 1973) Vol. 1, p. 93.
45) G. E. P. Box and M. E. Muller, Ann. Math. Stat. **29**, 610 (1958).
46) Y. Hashimoto, N. Akashi, and J. Kushibiki, Tech. Rep. IEICE **97**, 37 (1997).